



**Photoelectrochemical Evidence of Nitrogen Incorporation
during Anodizing of Sputtering - Deposited Al-Ta Alloys**

Journal:	<i>Physical Chemistry Chemical Physics</i>
Manuscript ID	CP-ART-07-2015-004347.R3
Article Type:	Paper
Date Submitted by the Author:	17-Nov-2015
Complete List of Authors:	Zaffora, Andrea; Università di Palermo, Electrochemical Materials Science Laboratory, DICAM Santamaria, Monica; Università di Palermo, Electrochemical Materials Science Laboratory, DICAM Di Franco, Francesco; Università di Palermo, Electrochemical Materials Science Laboratory, DICAM Habazaki, Hiroki; Hokkaido University, Graduate School of Chemical Sciences and Engineering Di Quarto, Francesco; Università di Palermo, Electrochemical Materials Science Laboratory, DICAM



Journal Name

ARTICLE

Photoelectrochemical Evidence of Nitrogen Incorporation during Anodizing of Sputtering - Deposited Al-Ta Alloys

A. Zaffora,^a M. Santamaria,^{*a} F. Di Franco,^a H. Habazaki^b and F. Di Quarto^a

Received 00th January 20xx,
Accepted 00th January 20xx

DOI: 10.1039/x0xx00000x

www.rsc.org/

Anodic films were grown to 20 V on sputtering-deposited Al-Ta alloys in ammonium baborate and borate buffer solutions. According to Glow Discharge Optical Emission Spectroscopy, anodizing in ammonium containing solution leads to the formation of N containing anodic layers. Impedance measurements did not evidence significant differences between the dielectric properties of the anodic films as a function of the anodizing electrolyte. Photoelectrochemical investigation allowed to evidence that N incorporation induces a redshift in the light absorption threshold of the films due the formation of allowed localized states inside their mobility gap. The estimated Fowler threshold for electrons internal photoemission processes resulted to be independent on the anodizing electrolyte confirming that N incorporation doesn't affect appreciably the density of states distribution close to the conduction band mobility edge. Transport of photogenerated carriers has been rationalized according to Pai-Enck model of geminate recombination.

Introduction

The anodizing of aluminium and tantalum has been extensively studied due to the widespread use of the corresponding oxides as dielectric in electrolytic capacitor.^{1,2} In last decade, it has been proved that anodizing sputtering-deposited aluminium - tantalum alloys is a viable tool to grow Al-Ta mixed oxides, whose composition is a function of Al/Ta ratio in the base alloy. In refs. 3-5 the structure, composition and physico-chemical properties of such mixed oxides have been widely investigated. Transmission electron micrographs of ultramicrotomed sections revealed that anodic oxides on Al-Ta alloys are amorphous and uniform in thickness, with flat metal/oxide and oxide/electrolyte interfaces. They show nanometric roughness as also confirmed by Atomic Force Microscopy.⁵ The compositional depth profiles provided by Rutherford Back Scattering revealed the formation of oxides with uniform composition.^{3,4} The oxides growth resulted to occur due to simultaneous migrations of cations (Al^{3+} and Ta^{5+}) outwards and anions (O^{2-}) inwards proceeding in a cooperative manner, developing film material both at the film/electrolyte and metal/film interfaces, respectively. However, films structure and composition are also dependent upon the electrolyte due to possible incorporation of foreign species from anodizing bath.⁶⁻⁸ This is very important if we consider that the presence of foreign species in anodic films could affect

the electronic properties of the films with possible detrimental effects on dielectric properties of the oxides.

In refs. 9-11 it was shown that during anodizing in ammonium containing solutions of valve metals such as Nb, Ta and Ti, N incorporation occurs, with significant effects on the solid state properties of the corresponding oxides. More interestingly, in the case of tantalum, such incorporation is reported to occur only when the electrolyte pH was higher than the pH of zero charge (pH_{pzc}) of Ta_2O_5 , since negatively charged oxide surface allowed ammonium cations reaching the film and being deprotonated by the imposed electric field.

In this work we want to study if N incorporation occurs during the anodizing of Al-Ta alloys of different composition in ammonium baborate solution. Glow discharge optical emission spectroscopy is used to directly assess the presence of N into the anodic films, while the possible effect on the solid state properties is studied by impedance measurements and photoelectrochemical experiments.

Experimental Section

Metallic substrates and oxides

Aluminium, tantalum and Al-Ta alloys (10, 18, 20, 30, 42, 62, 81, 91 at % of Ta) were deposited by dc magnetron sputtering on glass substrates. The deposition was carried out in a Shimadzu, SP-2C system, at a rate of 0.11 nm s^{-1} , by using an Al target 99.99 % and a Ta target 99.9 %; the chamber was initially evacuated to 5×10^{-7} mbar with subsequent sputtering using Ar at 3×10^{-3} mbar.

The anodizing was undertaken in a borate buffer (0.42 M H_3BO_3 , 0.08 M $\text{Na}_2\text{B}_4\text{O}_7$) (pH = 8) and in 0.1 M ammonium baborate tetrahydrate (ABE, $(\text{NH}_4)_2\text{B}_4\text{O}_7 \cdot 4\text{H}_2\text{O}$) (pH ~ 9) at room temperature potentiodynamically at 10 mV s^{-1} . Alloys were

^a Electrochemical Materials Science Laboratory, DICAM, Università di Palermo, Viale delle Scienze, Ed. 6, Palermo, Italy. E-mail: monica.santamaria@unipa.it

^b Graduate School of Chemical Sciences and Engineering, Hokkaido University, Sapporo, Hokkaido, Japan.

Electronic Supplementary Information (ESI) available: [details of any supplementary information available should be included here]. See DOI: 10.1039/x0xx00000x

Tab. 1. Anodic films thicknesses

Base alloy	Thickness / nm
Al	24.0
Al-10at.%Ta	24.4
Al-18at.%Ta	25.1
Al-20at.%Ta	25.3
Al-30at.%Ta	26.2
Al-42at.%Ta	27.2
Al-62at.%Ta	28.9
Al-81at.%Ta	30.5
Al-91at.%Ta	31.4
Ta	32.4

anodized to 20 V vs. mercury/mercury oxide electrode (0 V vs. Hg/HgO = 0.098 V vs. SHE). The thickness of the anodic layers, estimated according to the anodizing ratio reported in previous works,^{3,4} are reported in Tab. 1.

X-Ray Reflectivity Measurements

X-Ray Reflectivity (XRR) spectra were collected using a Rigaku SmartLab X-ray diffractometer with a copper anode (Cu K α radiation, $\lambda = 0.15405$ nm, 30 kV, 20 mA). XRR spectra were recorded over the 2θ angle range from 0 to 4 with a step size of 0.0004° . Rigaku GlobalFit was used to fit the spectra.

Glow Discharge Optical Emission Spectroscopy

Elemental depth profile analysis was conducted by glow discharge optical emission spectroscopy (GDOES) using a Jobin Yvon 5000 instrument in an argon atmosphere of 600 Pa by applying RF of 13.56 MHz and power of 30 W with a pulse mode of 100 Hz and a duty cycle of 0.1 s. The wavelengths of the spectral lines used were 396.157, 302.017, 149.262, 249.678 and 130.217 nm for aluminium, tantalum, nitrogen, boron and oxygen respectively.

Impedance Measurements Setup

Impedance measurements were carried out in 0.25 M Na₂HPO₄ (pH \sim 9) through a Parstat 2263 (PAR), connected to a computer for the data acquisition. A Pt net with a very high specific surface was used as counter electrode, while a mercury/mercury oxide as reference electrode. The impedance spectra were generated by superimposing to the continuous potential a sinusoidal signal of amplitude 10 mV over the frequency range 100 kHz – 100 mHz. and the results were fitted with ZSimp software.

Photoelectrochemical Measurements Setup

The experimental set-up for photoelectrochemical investigations has been described elsewhere.¹² A 450W UV-VIS xenon lamp, coupled with a monochromator, allows irradiation of the specimen through a quartz window. A two phase lock-in amplifier, coupled with a mechanical chopper (with a frequency of 13 Hz) enables the separation of the photocurrent from the total current circulating in the cell. Photocurrent spectra reported are corrected for the relative photon flux of the light source at each wavelength, so that the

photocurrent yield is represented in the y axis in arbitrary current units. All the experiments were performed in air at room temperature in 0.1 M ABE.

Results

Anodic Films Growth

Anodic films were grown to 20 V at 10 mV s^{-1} on all investigated alloys. In Fig. 1a we report the growth curve relating to the anodizing of Al-91at.%Ta alloy. As typical of valve metals, after an abrupt increase, the current density reaches an almost constant value, which is a function of the metallic substrate composition. The current density is sustained by the oxidation of metals, according to the following half cell reaction:



where Me is Al and/or Ta depending of alloy composition. According to Faraday's law in the case of high field growth of

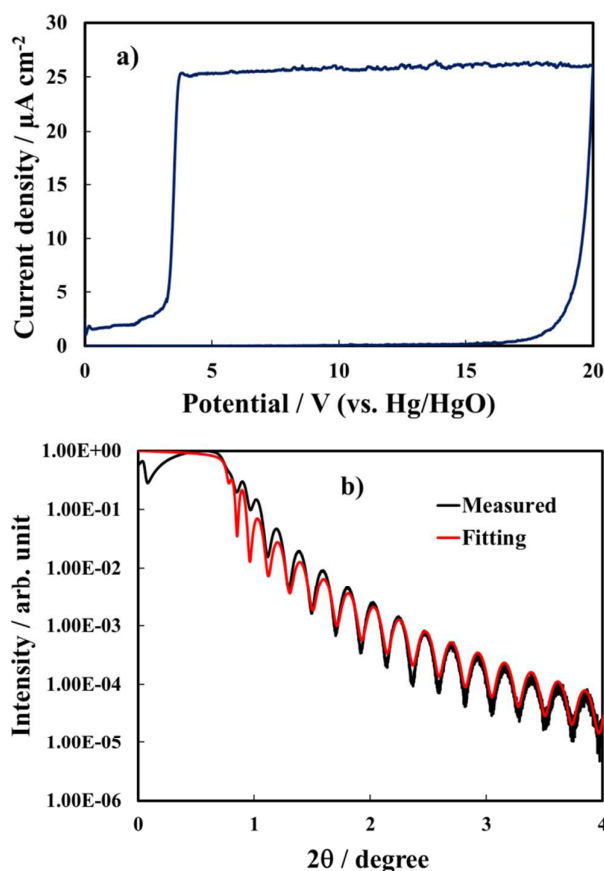


Fig. 1. a) Current density vs potential curves recorded during the potentiodynamic growth of anodic film on Al-91at.%Ta alloy at 10 mV s^{-1} in 0.1 M ABE. b) X-Ray Reflectivity spectrum relating to 20 V anodic film grown on Al-91at.%Ta. Fitting parameters: density = 8.5 g cm^{-3} , thickness = 37 nm, roughness = 0.33 nm.

anodic films, it is possible to relate the electric field strength, E , to the growth rate, dV/dt , according to equation:

$$\frac{dV}{dt} = \eta \frac{iEM}{zF\rho} \quad (2)$$

in which i is the measured current density, M is the molecular weight of the growing oxide, z the number of electrons circulating per mole of formed oxide, F the Faraday constant, ρ the film density and η the growth efficiency. η is defined as:

$$\eta = \frac{i_{\text{form}}}{i_{\text{tot}}} = \frac{i_{\text{form}}}{i_{\text{form}} + i_{\text{diss}} + i_{\text{el}}} \quad (3)$$

where i_{form} is the current density effectively employed for the film formation, i_{diss} is the current density fraction due to dissolution phenomena, expected to be negligible for all the investigated samples according to the Pourbaix diagrams relating to Al and Ta,¹³ and i_{el} is the electronic current which is negligible due the blocking character of the oxides, as confirmed by the very low current circulating during the reverse scan (see Fig. 1a).

In Fig. 1b we report the XRR spectrum relating to anodic film of Fig. 1a. The resulting angle-dependent curve, which is correlated to changes of the electron density in the sample, was fitted with a triple layer model (SiO₂/Alloy/Oxide). The fitting procedure allowed to estimate a film thickness very close to that estimated from the anodizing ratio (see Tab. 1), and a density which is very close to that reported for pure anodic Ta₂O₅³ with roughness in order of few Å. The roughness factor resulted between 0.3 and 0.5 nm for the investigated samples.

Oxide thickness increases due to chemical reaction between Ta⁵⁺, Al³⁺, O²⁻. Mobile cationic species are produced at the metal/oxide interface and migrate outward toward the

oxide/electrolyte interface. Mobile anionic species are produced at the oxide/electrolyte interface and migrate inward. In aqueous solution, where water molecules might be expected to adhere to the film with negatively charged oxygen atom adjacent to the oxide surface, mobile anionic species are mainly O²⁻ and OH⁻ ions derived from water deprotonation.^{14,15} The OH⁻, once incorporated, are converted to O²⁻ ions and protons, with H⁺ migrating out of the film under the high electric field. If large oxyanions are present in the anodizing bath (e.g. baborate), hydrogen bonds can be formed between H of water molecules and O of such oxyanions (see Scheme 1) with a consequent weakening of O-H covalent bonds in H₂O and, thus, easier de-protonation. However, it has been proved that other anionic species, A^{y-}, of the anodizing bath can be also incorporated during the anodizing process, leading to the formation of oxides containing foreign species.¹⁶ Their distribution along the film thickness is a function of the relative migration rate of A^{y-} with respect to O²⁻/OH⁻ ions. More specifically, incorporation of several inorganic¹⁷ and organic^{18,19} anions has been reported during the anodizing of Al, while incorporation of several ions has been proved during the anodizing of Ta.²⁰ Recently, it has been also demonstrated that N incorporation occurs during the anodizing of tantalum in ammonium baborate solutions, provided that the electrolyte pH is higher than the pH of zero charge (pH_{pzc}) of the oxide. In the latter case oxide surface is negatively charged, thus allowing NH₄⁺ ions to approach the oxide/electrolyte interface and to be de-protonated generating NH_{3-x}^{x-} moieties that are incorporated into the anodic film with the consequent formation of a oxynitride.¹⁰ In Fig. 2 we report GDOES elemental depth profiles relating to anodic films grown to 20 V in 0.1 M ABE on Al-10at.%Ta, Al-42at.%Ta and Al-81at.%Ta alloys. N signal is weak but present across the whole film thickness, thus confirming that nitrogen incorporation occurs also during the anodizing of Al-Ta alloys. In refs. 21 and 22 pH_{pzc} of ~ 9.5 and 2.9 are reported for alumina and tantalum, respectively. Therefore, we expect that the higher is Al content into the oxide, the lower is the extent of the incorporation phenomena (see Fig. 2).

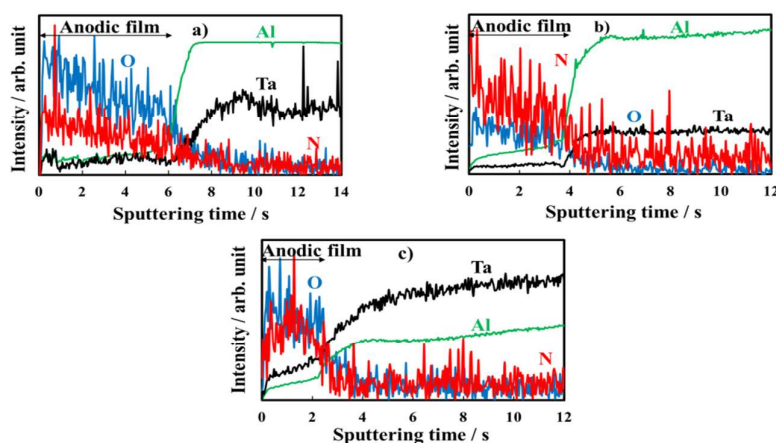
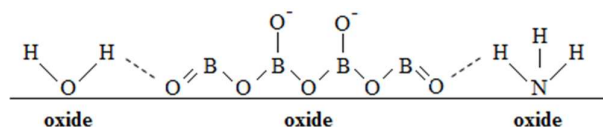


Fig. 2. GDOES depth profiles of the anodic films grown to 20 V on (a) Al-10at.%Ta, (b) Al-42at.%Ta and (c) Al-81at.%Ta alloys in 0.1 M ABE.



Scheme 1.

Formation of $\text{NH}_3^{\text{x-}}$ moieties is assisted by weakening of the N-H bond as depicted in Scheme 1 since, due to the large electronegativity of nitrogen, formation of hydrogen bonds between H of ammonia and O of oxyanions (i.e. $\text{-NH}\cdots\text{O}$) can also occur. As occurs for OH^- , $\text{NH}_3^{\text{x-}}$ can lose protons and being finally incorporated into the anodic films as N^{3-} ions. N-H dissociation energy in ammonia (388 kJ mol^{-1}) is lower than O-H dissociation energy in water (463 kJ mol^{-1}). Moreover, ionic radii of NH_2^- and N^{3-} (0.173 nm and 0.171, respectively according to refs. 23 and 25) are close to that of O^{2-} and OH^- (0.140 nm and 0.153 nm, respectively), and even lower than that of oxyanions, whose incorporation has been proved in previous works (e.g. 0.238 nm for PO_4^{3-} and 0.230 nm for SO_4^{2-} , see ref. 20). Thus, it is likely that a oxynitride can be formed during anodizing process without significant structural problems, considering that the films are amorphous and that according to the literature the only effect of nitridation of crystalline tantalum oxide is an expansion of the lattice, due to the smaller ionic radius of O^{2-} (0.140 nm) with respect to N^{3-} (0.171 nm).²⁴ Such expansion is also reported to occur for N-doped Ta_2O_5 and in spite of this, a crystalline stable phase is formed.

Impedance Measurements

In order to get information on the dielectric properties of the investigated oxides, we recorded electrochemical impedance spectra and differential capacitance curves. In Fig. 3a,b,c we report the EIS spectra, recorded in 0.25 M Na_2HPO_4 at $U_E = 5 \text{ V}$ (Hg/HgO) (i.e. at potential more anodic than the corresponding flat band potential, see below), in Modified Bode representation relating to the anodic films grown on Al-42at.%Ta, Al-62at.%Ta and Al-91at.%Ta alloys respectively, in 0.1 M ABE and borate buffer to 20 V. As shown in the Fig. 3, no significant differences are found in EIS spectra due to the anodizing electrolyte. The high $|Z|$ and a phase angle very close to 90° , confirm the formation of blocking oxides. Spectra can be simulated by the electrical circuit reported in Fig. 3d, where R_{el} is the electrolyte resistance (employed to get the Modified Bode representation), R_{ox} is the anodic film resistance and Q_{ox} is a Constant Phase Element (CPE) introduced to model the oxide capacitance.

Another RQ parallel was inserted to model the electrochemical reaction, where R_{ct} is the charge-transfer resistance and Q_H the non ideal Helmholtz double layer capacitance. This equivalent circuit very well fits the experimental data relating to the all anodic films grown in 0.1 M ABE, with the fitting parameters reported in Tab. 2. The very high R_{ox} values and α very close to 1 suggest that the oxides behave like ideal capacitors. It is interesting to mention that very high R_{ct} were estimated, as expected for blocking interface, and Q_H allowed to estimate double layer capacitance very close to $20 \mu\text{F cm}^{-2}$, the value reported in the literature for aqueous solutions.²⁶

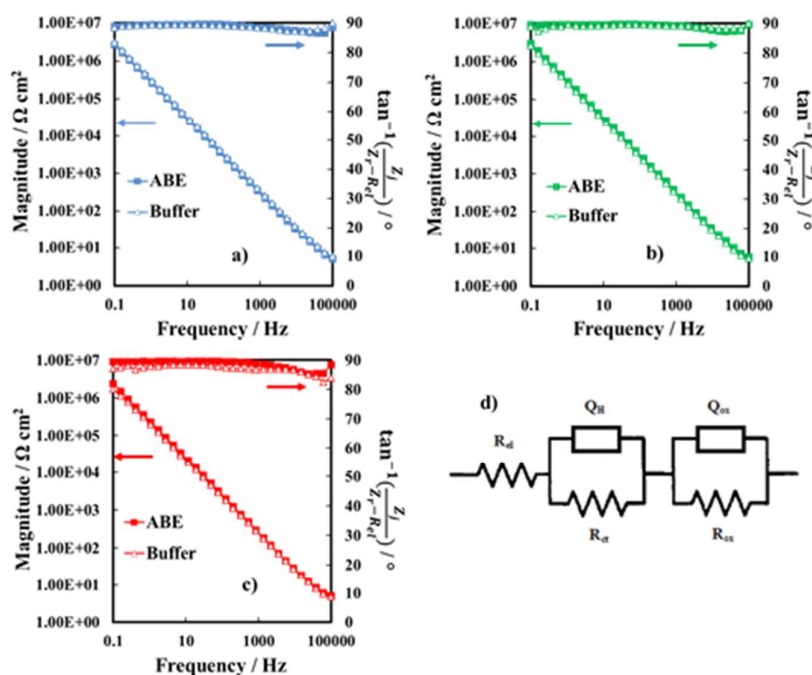


Fig. 3. EIS spectra relating to anodic films grown on (a) Al-42at.%Ta, (b) Al-62at.%Ta and (c) Al-91at.%Ta alloys in ABE and borate buffer, recorded by polarizing the film at 5 V vs Hg/HgO. (d) Electrical equivalent circuit employed to model metal/oxide/electrolyte interfaces.

Tab. 2. Fitting parameters relating to EIS spectra of the all investigated anodic films using equivalent electric circuit of Fig. 3d.

Base alloy	$R_{el} / \Omega \text{ cm}^2$	$R_{ct} / \Omega \text{ cm}^2$	$Q_H / S \text{ s}^\alpha \text{ cm}^2$	α	$R_{ox} / \Omega \text{ cm}^2$	$Q_{ox} / S \text{ s}^\alpha \text{ cm}^2$	α
Al	14	1×10^4	2.1×10^{-5}	0.82	1×10^5	4.3×10^{-7}	1
Al-10at.%Ta	15	1×10^6	2.3×10^{-5}	0.85	1×10^8	4.4×10^{-7}	0.99
Al-18at.%Ta	14	1×10^6	2.1×10^{-5}	0.80	1×10^8	5.4×10^{-7}	1
Al-20at.%Ta	39	1×10^6	2.4×10^{-5}	0.87	1×10^9	4.2×10^{-7}	0.99
Al-30at.%Ta	26	1×10^6	2.5×10^{-5}	0.88	9×10^9	4.4×10^{-7}	0.99
Al-42at.%Ta	20	1×10^6	2.2×10^{-5}	0.88	1×10^8	6.2×10^{-7}	0.99
Al-62at.%Ta	24	1×10^6	2.2×10^{-5}	0.85	1×10^8	5.4×10^{-7}	0.99
Al-81at.%Ta	23	1×10^6	2.0×10^{-5}	0.82	1×10^8	7.8×10^{-7}	1
Al-91at.%Ta	27	4×10^6	2.2×10^{-5}	0.95	1×10^9	6.9×10^{-7}	0.99
Ta	39	1×10^6	2.2×10^{-5}	0.88	1×10^8	8.5×10^{-7}	1

In Fig. 4 we report the differential capacitance measurements, recorded at $f = 1$ kHz, for all the investigated films. It is evident that the capacitance is almost potential independent and slightly dependent on frequency, as expected for amorphous insulating materials.²⁶ A comparison with the capacitance of 20 V anodic films on Al-Ta alloys grown in borate buffer solution shows that not appreciable differences are evident on the overall impedance (Fig. 5a,b,c). This suggests that the presence of N into the oxide causes the formation of deep localized states, thus at energy level so far from the conduction band mobility edge that they cannot contribute to the measured capacitance in the range of investigate frequency. This is agreement with previous experimental findings on the effect of nitrogen incorporation during the anodizing of Ta and Ti,^{10,11} which is reported to induce formation of localized states close to the valence band mobility edge.

Provided that the equivalent circuit of Fig. 3d well simulates the impedance of the overall metal/oxide/electrolyte interface, it is easy to extract the oxide capacitance from C_M . Assuming that C_{ox} can be described by a parallel plate capacitor model:

$$C_{ox} = \frac{\epsilon_r \epsilon_0}{d_{ox}} \quad (4)$$

where ϵ_0 (8.85×10^{-14} F cm^{-1}) is the vacuum permittivity, ϵ_r the film relative permittivity and d_{ox} its thickness. Whereas there are no differences in anodic film growth with respect to anodizing solutions, oxides thicknesses reported in Tab. 1 can be considered in calculating ϵ_r for the oxides grown in 0.1 M ABE. Dielectric constants are reported in Tab. 3 and the values are in very good agreement with that reported for the oxides grown in borate buffer.

Photoelectrochemical Measurements

In order to study the influence of N incorporation on the solid state properties of the oxides, photoelectrochemical measurements were carried out. Anodic photocurrent spectra (normalized for the maximum value of I_{ph}), relating to the anodic film grown to 20 V on Al-62at.%Ta alloy in both solutions recorded by polarizing the electrodes at 5 V

(Hg/HgO) are reported in Fig. 6a. An evident redshift in the optical absorption threshold is present for the anodic film grown in 0.1 M ABE, while no photocurrent is detected for $\lambda \geq 310$ nm in the spectrum relating to the oxide grown in borate buffer. From photocurrent spectra, it is possible to estimate the optical band gap value of the investigated anodic films according to the following equation:

$$(I_{ph}hv)^n \propto (hv - E_g) \quad (5)$$

valid for photon energy in the vicinity of the band gap. I_{ph} is the photocurrent yield, assumed proportional to the light absorption coefficient, hv is the photon energy, E_g the optical band gap and n value equal to 0.5 has been assumed for non direct optical transitions.¹²

It is important to mention that due to the amorphous structure of the investigated oxides, presence of allowed localized states inside the gap is predicted according to several models of density of states distribution,¹² thus it is more appropriate to define E_g in eq 5 as the mobility gap of the layer. An E_g of 4.2 eV has been estimated for the anodic film grown in buffer, as shown in Fig. 6c, which is slightly lower than that estimated for thinner oxides (i.e. formation voltage = 10 V).²⁷ For the oxide grown in the ammonium-containing solution (Fig. 6b) by extrapolating to zero the $(I_{ph}hv)^{0.5}$ vs hv plot it was possible to estimate an E_g of ~ 4.1 eV but a long photocurrent tail is also present ending at 3.4 eV.

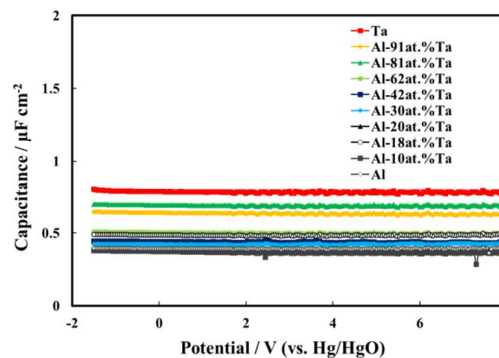


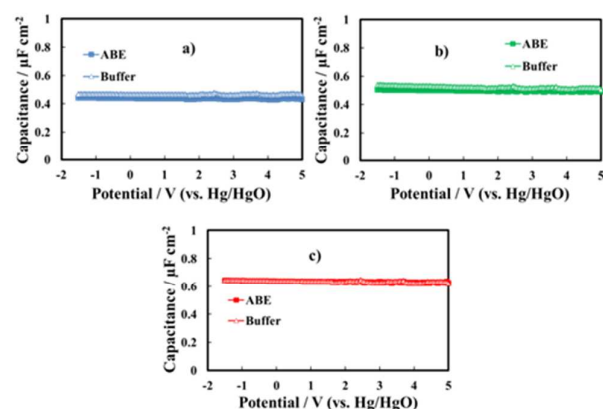
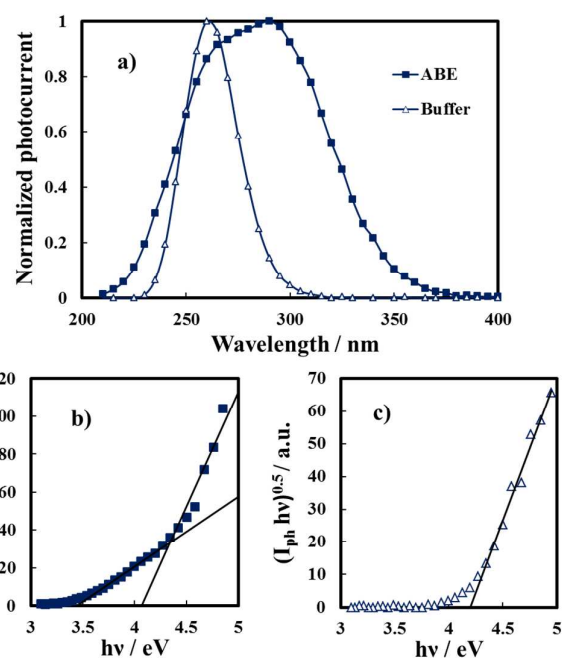
Fig. 4. Measured series capacitance relating to all oxides grown up to 20 V vs. Hg/HgO in ABE. a.c. signal frequency: 1 kHz.

Tab. 3. Anodic films dielectric constants estimated from differential capacitance measurements.

Base alloy	Dielectric constant
Al	9
Al-10at.%Ta	10
Al-18at.%Ta	14
Al-20at.%Ta	12
Al-30at.%Ta	13
Al-42at.%Ta	14
Al-62at.%Ta	16
Al-81at.%Ta	24
Al-91at.%Ta	23
Ta	29

The latter is due to optical transitions involving allowed states in the mobility gap of the oxide, generated by N incorporation. The same photoelectrochemical behaviour was shown by anodic films grown on Al-Ta alloys with a Ta content ≥ 42 at.%, (see Fig. 7), while for oxide grown on Al-20at.%Ta there is no evidence of photocurrent at energy lower than E_g of the oxide. We want to mention that no anodic photocurrent was measured with anodic films grown on Al-Ta alloys with a lower Ta content.

We have also studied the dependence of the measured photocurrent on the applied potential, i.e. on the electric field strength across the films. In Fig. 8a we show the I_{ph} vs U_E curves (photocharacteristics) for the anodic films grown on Al-62at.%Ta to 20 V in both ABE and borate buffer, recorded at $\lambda = 270$ nm ($h\nu = 4.58$ eV). As it will be better discussed in the next Section, the shape of I_{ph} vs U_E curves suggests the occurrence of recombination phenomena for both films grown in ABE and borate buffer. As expected for insulating films, by scanning the electrode potential toward the cathodic direction, a clear inversion of the photocurrent sign was revealed, as confirmed by a sharp change in the photocurrent phase angle (not reported).

**Fig. 5.** Measured series capacitance relating to the anodic films grown on (a) Al-42at.%Ta, (b) Al-62at.%Ta and (c) Al-91at.%Ta alloys in ABE and borate buffer. A.c. signal frequency: 1 kHz.**Fig. 6.** Anodic photocurrent spectra (a) relating to anodic films grown on Al-62at.%Ta alloy in ABE and borate buffer, recorded by polarizing the electrodes at 5 V vs. Hg/HgO. Band gap estimate by assuming non direct optical transitions relating to the same anodic films grown in ABE (b) and borate buffer (c).

In the case of insulating material both anodic and cathodic photocurrent can be measured when polarizing potential is more anodic and more cathodic than the flat band potential, U_{FB} , of the oxide, respectively.

In order to estimate U_{FB} for the investigated layers, current vs time measurements were carried out under constant irradiating wavelength and manually chopping the irradiation. Fig. 9 shows current transients relating to the anodic film grown on Al-91at.%Ta alloy in ABE at two different polarizing potentials. Under strong anodic polarization, i.e. at 8 V (Hg/HgO) (Fig. 9a), soon after irradiation the current reaches an almost stationary value for all the investigated wavelengths (up to $\lambda = 360$ nm).

At $U_E = -0.8$ V (Hg/HgO) (Fig. 9b), in spite of the presence of anodic photocurrent spikes soon after irradiation, stationary photocurrent is cathodic, thus suggesting $U_{FB} > -0.8$ V (Hg/HgO). At this electrode potential, the electric field is not high enough to avoid photocarriers recombination preventing cathodic photocurrent detection at $\lambda = 360$ nm, i.e. at photon energy lower than the mobility gap.

U_{FB} values estimated from current - time transients for anodic films grown on alloys with Ta content ≥ 62 at.% are reported in Tab. 4. For anodic films grown in 0.1 M ABE with a Ta content ≥ 62 at.%, it was possible to record photocharacteristics under illumination with photons corresponding to $h\nu$ lower than their mobility gap. In Fig. 8b we show the I_{ph} vs U_E at $\lambda = 330$ nm ($h\nu = 3.75$ eV) for the anodic film grown on Al-62at.%Ta to 20 V in ABE.

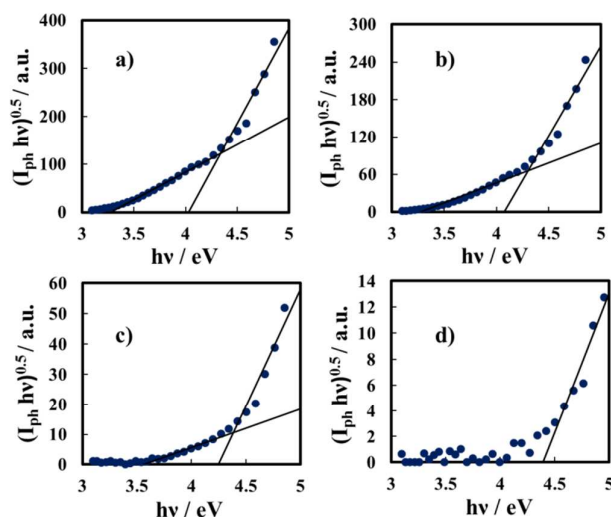


Fig. 7. Band gap estimate by assuming non direct optical transitions relating to anodic films grown to 20 V on (a) Al-91at.%Ta, (b) Al-81at.%Ta, (c) Al-42at.%Ta, and (d) Al-20at.%Ta alloys in ABE.

I_{ph} decreases during the potential scan toward cathodic direction and for $U_E < U_{FB}$ cathodic photocurrent is measured, as evidenced in the magnified area of the plot. Thus, photocurrent spectra were recorded at potential lower than U_{FB} (i.e. at -1.5 V vs Hg/HgO), as shown in Fig. 10a for oxides grown on Al-62at.%Ta alloy in both ABE and borate buffer solutions. As already found for several insulating oxides²⁸⁻³³ as well as for thinner films grown in ammonium free electrolyte on Al-Ta alloys,²⁷ a long photocurrent tail appears that has been explained by electrons injection processes from the alloy Fermi level to the oxide conduction band (see Fig. 10d). The threshold energy, E_{th} , associated to this process can be estimated according to Fowler's law:²⁸

$$(I_{ph})^{0.5} \propto (hv - E_{th}) \quad (6)$$

from the long wavelength region of the photocurrent spectra, corresponding to $\lambda \geq 400$ nm, which has been recorded using a 400 nm cut off filter to avoid doubling effect (see Fig. 10b). The same internal photoemission process occurs for the anodic film grown in ABE with a Fowler threshold almost coincident with that estimated for N free oxide. This experimental finding further supports that N incorporation induces formation of allowed states close to valence band mobility edge of the anodic films without significant effects on the density of states close to the conduction band mobility edge.

Discussion

In the frame of Butler-Gartner model, for crystalline insulating films, a linear dependence of the measured photocurrent on the applied potential is expected in absence of trapping phenomena, which can modify the electric field distribution across the layer.³⁴

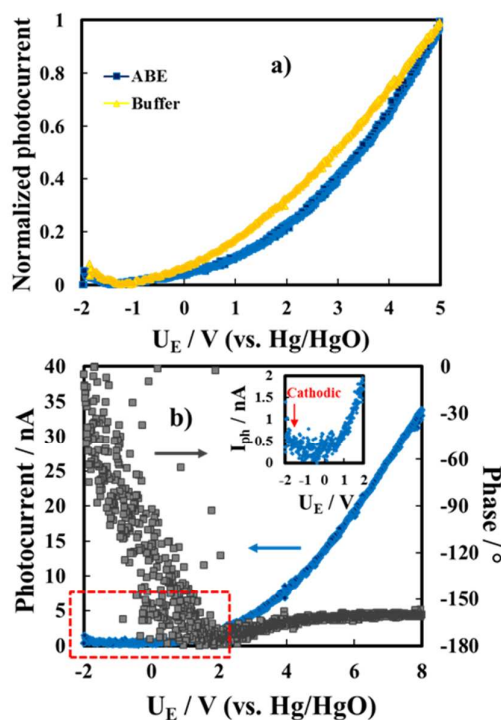


Fig. 8. (a) Photocurrent vs potential curves relating to 20 V anodic films grown on Al-62at.%Ta alloy in ABE and borate buffer recorded in 0.1 M ABE at $\lambda = 270$ nm. (b) Photocurrent vs potential curve relating to the oxide grown on Al-62at.%Ta alloy in ABE at $\lambda = 330$ nm. Potential scan rate: 10 mV/s.

However, for both anodic films grown in ABE and buffer, such dependence is not linear supporting the presence of recombination phenomena. For amorphous material the lack of long range order induces the formation of allowed localized states close to the mobility edge of the oxide, in agreement with the Mott and Davis model.³⁵ Thus, together with surface and bulk recombination phenomena expected for both crystalline and amorphous materials, we have to account for the occurrence of geminate recombination phenomena which reduce the efficiency of free carrier generation for amorphous anodic film on Al-Ta alloys. Geminate recombination occurs generally in any material where the photogenerated carriers display very low mobility.

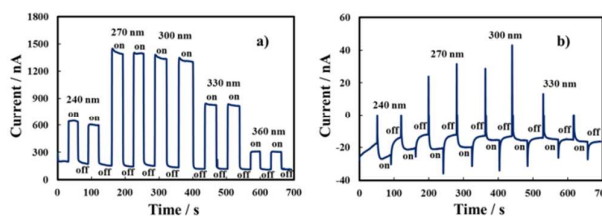


Fig. 9. Total current circulating under irradiation (on) and in the dark (off) in the oxide grown on Al-91at.%Ta alloy in ABE, by polarizing the electrode at 8 V (a) and -0.8 V (b) vs. Hg/HgO at different wavelengths.

Tab. 4. Flat band potential values estimated by recording current transients under constant irradiating wavelength relating to the anodic oxides with a Ta content ≥ 62 at.%.

Base alloy	U_{fb} / V (vs. Hg/HgO)
Al-62at.%Ta	-0.70
Al-81at.%Ta	-0.75
Al-91at.%Ta	-0.70
Ta	-0.65

The mobility of carriers in the localized states (below the conduction band and above the valence band edges) is much lower than in the extended states, so the probability of initial recombination effects in amorphous materials is quite high.

In fact, during the thermalization time, the electron-hole pairs do not cover a distance long enough to prevent recombination due to their mutual coulombic attraction. Owing to this insufficient separation, a certain fraction of the photogenerated carriers recombine before the transport process can separate them permanently.^{36,37}

To explain the dependence of photocurrent on both the applied potential and irradiating wavelength, we recall Onsager's theory,³⁸ originally developed for weak electrolytes, and then applied by Pai and Enck to the initial recombination process (geminate recombination) of electron-hole pairs in amorphous selenium.³⁹ This was achieved deriving a mathematical expression for the efficiency of photogeneration, η_g , taking into account the tri-dimensional aspect of the generation and the effect of the electric field on the initial separation of the photocarriers:

$$\eta_g(r_0, E) = \frac{kT}{eEr_0} e^{-A} e^{-eEr_0/kT} \times \sum_{m=0}^{\infty} \frac{A^m}{m!} \sum_{n=0}^{\infty} \sum_{l=m+n+1}^{\infty} \left(\frac{eEr_0}{kT} \right)^l \frac{1}{l!} \quad (7)$$

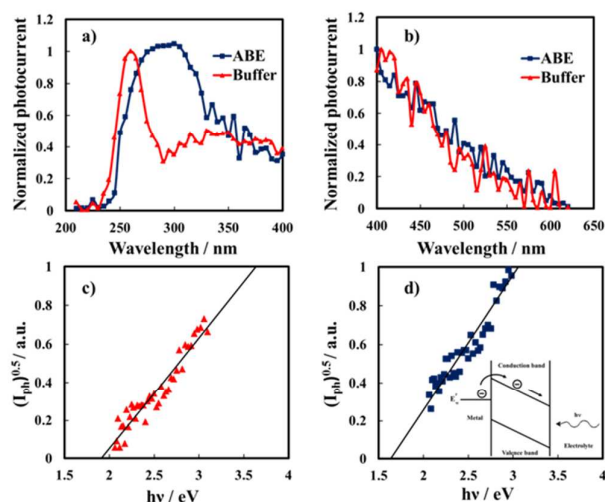


Fig. 10. (a) Cathodic photocurrent spectra relating to the oxides grown on Al-62at.%Ta alloy in ABE and borate buffer recorded at -1.5 V vs. Hg/HgO as electrode potential. (b) Long wavelength region of the photocurrent spectra, recorded by using a UV filter. Fowler plots relating the oxide grown in buffer (c) and in ABE (d). Inset: electrons internal photoemission from metal Fermi level.

where E the electric field, k the Boltzmann constant, e the electronic charge, $A = e^2/4\pi\epsilon\epsilon_0kTr_0$, ϵ the oxide dielectric constant and by considering that every absorbed photon creates a pair of thermalized carriers bound by their mutual coulombic attraction. r_0 is the thermalization length, i.e. the distance travelled by the photocarriers before their effective separation by the electric field. In eq 7 the only parameter that changes with irradiating photon wavelength is r_0 , which is a function of the excess energy $\Delta E = (h\nu - E_{trans})$, i.e. the extra with respect to that necessary for the optical transition. During the thermalization process, this excess energy is dissipated over the local potential by phonons emission.³⁹ According to eq 7, higher generation efficiencies can be obtained with high electric fields and high thermalization lengths. Since r_0 directly depends on photon energy, high efficiency values are achieved at short irradiation wavelengths, while strong geminate recombination effects are characteristic of photogeneration at high irradiation wavelengths. η_g can be introduced in the general expression of photocurrent on applied potential, i.e. applied electric field:

$$I_{ph} = \eta_g e \Phi_0 (1 - R) \left[1 - \exp\left(-d_{ox} \frac{1 + \alpha L_D}{L_D}\right) \right] \frac{\alpha L_D}{1 + \alpha L_D} \quad (8)$$

where Φ_0 is the incident photon flux on the oxide surface, R is the reflection coefficient, α is the absorption coefficient, d_{ox} is the anodic film thickness, L_D is the sum of drift lengths of injected photocarriers, expressed as:

$$L_D = (\mu_h \tau_h + \mu_e \tau_e) E \quad (9)$$

with μ photocarriers mobility and τ photocarriers lifetime.¹² Eq 8 has been used to fit photocharacteristics relating to anodic films grown on Al-62at.%Ta, Al-81at.%Ta, Al-91at.%Ta alloys and on pure Ta to 20 V in 0.1 M ABE. In Fig. 11 fitting curves are overlapped to the photocharacteristics relating to the anodic films grown on Al-62at.%Ta, Al-81at.%Ta and Al-91at.%Ta alloys, recorded at two different wavelengths, 240 nm and 330 nm, corresponding to irradiating photon energy higher and lower than oxides band gap.

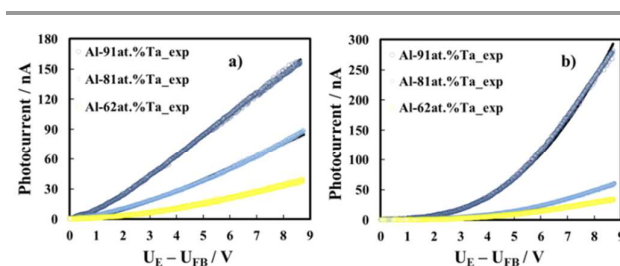


Fig. 11. Photocurrent vs band bending relating to anodic films grown to 20 V on Al-91at.%Ta, Al-81at.%Ta, and Al-62at.%Ta alloys in ABE, recorded at $\lambda = 240$ nm (a) and $\lambda = 330$ nm (b). Continuous lines are plotted according to eq 8 with the fitting parameters of Tab. 5.

The reflection coefficient has been calculated by using a three layers model (i.e. solution/oxide/metal) under normal light incidence and by including the effects of multiple reflections,⁴⁰ with optical constants for solution, metal and oxide taken from refs. 41 and 42. During fitting procedure we used the flat band potentials estimated from current time transients (see Tab. 4) and oxides' thickness calculated from the anodizing ratio estimated in refs. 3 and 4 by direct inspection of transmission electron micrographs of ultramicrotomed section (see Tab. 1). The best fitting parameters are summarized in Tab. 5. It is interesting to mention that r_0 is inversely proportional to wavelength, and that very low $\mu\tau$ values were derived from the best fitting procedure. This suggests that for λ corresponding to both supra and sub band gap values, photocarriers are generated in localized states. Due to the amorphous nature of the investigated anodic films, we expect that close to conduction and valence band mobility edges, lattice disorder and/or presence of not stoichiometric oxides induce the formation of localized states, which can extend up to 0.2 eV below CB and above VB edges.³⁰ For $h\nu < E_g$ we can conclude that allowed localized states are also present inside the mobility gap and $\mu\tau$ even lower than that estimated for higher irradiating wavelength suggest that they are strongly localized.

Tab. 5. Fitting parameters relating to photocharacteristics, recorded at different wavelengths in 0.1 M ABE, for anodic film grown to 20 V on Al-Ta alloys with Ta content ≥ 62 at. %.

Base alloy	Wavelength / nm	$\mu\tau / \text{cm}^2 \text{V}^{-1}$	$r_0 / \text{\AA}$
Al-62at.%Ta	240	6.7×10^{-15}	10
	270	3.7×10^{-15}	7.5
	300	9.2×10^{-16}	7
	330	4.8×10^{-16}	6
Al-81at.%Ta	240	1.3×10^{-14}	10
	270	1.0×10^{-14}	6
	300	3.7×10^{-15}	4.5
	330	1.9×10^{-15}	4
Al-91at.%Ta	240	2.3×10^{-14}	14
	270	2.1×10^{-14}	7
	300	1.0×10^{-14}	5
	330	9.0×10^{-15}	4
Ta	240	2.4×10^{-14}	17.5
	270	1.9×10^{-14}	6
	300	9.0×10^{-15}	4
	330	7.7×10^{-15}	3

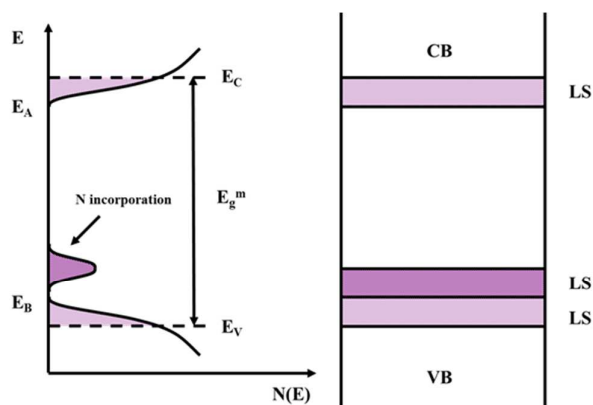


Fig. 12. Electronic structure of an amorphous semiconducting oxides following the Mott-Davis model with allowed localized states in the mobility gap. LS: localized states.

If we recall that Fowler threshold energies for films grown in borate buffer and films grown in ABE are almost coincident and that N incorporation does not contribute significantly to the measured impedance, we can suggest that anodizing in ABE leads to the formation of anodic films whose density of states can be described according to the sketch of Fig. 12. N incorporation induces the formation of allowed localized states close to the valence band mobility edge of the oxides, and that the energy distance of such states from conduction band mobility edge is roughly related to the redshift of the light absorption threshold of the anodic spectra.

Conclusions

Anodic films were grown to 20 V on sputtering – deposited Al-Ta alloys of several compositions in 0.1 M ABE and borate buffer solutions. According to GDOES compositional depth profiles, anodizing in ABE leads the formation of N containing oxide layers with nitrogen distributed across the whole film thickness. The presence of N does not change appreciably the impedance of the oxides, as suggested by the comparison between the impedance spectra and the differential capacitance curves relating to anodic films grown in ammonium-free and ammonium-containing solutions. In contrast, N incorporation significantly changes the photoelectrochemical behaviour of the anodic films grown on Al-Ta alloys with Al content ≥ 20 at.%. A redshift of the light absorption threshold of the investigated layers was evidenced, which is attributed to optical transition involving allowed states inside the mobility gap of the films. The dependence of photocurrent on photon energy and on the electric field strength in the frame of Pai-Enck model for geminate recombination, suggested that incorporation of nitrogen induces the formation of allowed localized states. Such states are close to the valence band mobility edge, since they do not contribute to the measured impedance up to very low frequency of the a.c. signal (0.1 Hz) and since they do not affect Fowler threshold for internal electron photoemission phenomena.

Notes and references

- 1 G. Scaduto, M. Santamaria, P. Bocchetta and F. Di Quarto, *Thin Solid Films*, 2014, **550**, 128.
- 2 S. Ezhilvalavan and T. Y. Tseng, *J. Mater. Sci.: Mater. Electron.*, 1999, **10**, 9.
- 3 H. Habazaki, K. Shimizu, P. Skeldon, G. E. Thompson and G. C. Wood, *Proc. Roy. Soc. A*, 1997, **453**, 1593.
- 4 G. Alcalá, S. Mato, P. Skeldon, G. E. Thompson, P. Bailey, T. C. Q. Noakes, H. Habazaki and K. Shimizu, *Corros. Sci.*, 2003, **45**, 1803.
- 5 G. Alcalá, P. Skeldon, G. E. Thompson, A. B. Mann, H. Habazaki and K. Shimizu, *Nanotechnology*, 2002, **13**, 451.
- 6 S. J. Garcia-Vergara, I. S. Molchan, F. Zhou, H. Habazaki, D. Kowalski, P. Skeldon and G. E. Thompson, *Surf. Interface Anal.*, 2011, **43**, 893.
- 7 F. Zhou, D. J. Leclere, S. J. Garcia-Vergara, T. Hashimoto, I. S. Molchan, H. Habazaki, P. Skeldon and G. E. Thompson, *J. Electrochem. Soc.*, 2010, **157**, C437.
- 8 H. Habazaki, K. Shimizu, S. Nagata, P. Skeldon, G. E. Thompson and G. C. Wood, *Corros. Sci.*, 2002, **44**, 1047.
- 9 S. Ono, K. Kuramochi and H. Asoh, *Corros. Sci.*, 2009, **51**, 1513.
- 10 F. Di Franco, M. Santamaria, F. Di Quarto, E. Tsuji and H. Habazaki, *Electrochim. Acta*, 2012, **59**, 382.
- 11 S. Miraghaei, M. Santamaria and F. Di Quarto, *Electrochim. Acta*, 2014, **134**, 150.
- 12 (a) F. Di Quarto, F. La Mantia and M. Santamaria, in *Modern Aspects of Electrochemistry, No. 46: Progress in Corrosion Science and Engineering I*, eds. S.-I. Pyun and J.-W. Lee, Springer, New York, 2009; Chapter 4, pp. 231–316. (b) F. La Mantia, M. Santamaria, F. Di Quarto and H. Habazaki, *J. Electrochem. Soc.*, 2010, **157**, C258.
- 13 M. Pourbaix, *Atlas of electrochemical equilibria in aqueous solutions*, Pergamon Press, Oxford, U.K., 1966.
- 14 J. W. Diggle (ed.), *Oxides and Oxide Films*, Marcel Dekker, Inc., New York, 1973.
- 15 A. J. Brock and G. C. Wood, *Electrochim. Acta*, 1967, **12**, 395.
- 16 H. Habazaki, K. Fushimi, K. Shimizu, P. Skeldon and G. E. Thompson, *Electrochem. Commun.*, 2007, **9**, 1222.
- 17 G. C. Wood, P. Skeldon, G. E. Thompson and K. Shimizu, *J. Electrochem. Soc.*, 1996, **143**, 74.
- 18 F. Di Quarto, S. Piazza, A. Splendore and C. Sunseri, *Proceedings of the Symposium on Oxide Films on Metals and Alloys*, The Electrochemical Society, Inc., Pennington, 1992.
- 19 K. Shimizu, H. Habazaki, P. Skeldon, G. E. Thompson and G. C. Wood, *Electrochim. Acta*, 2001, **46**, 4379.
- 20 K. Shimizu, K. Kobayashi, G. E. Thompson, P. Skeldon and G. C. Wood, *Philos. Mag. B*, 1996, **73**, 461.
- 21 E. McCafferty, *Electrochim. Acta*, 2010, **55**, 1630.
- 22 E. McCafferty, *J. Electrochem. Soc.*, 1999, **146**, 2863.
- 23 A. F. Wells, *Structural Inorganic Chemistry*, Clarendon Press, Oxford, U.K., 1975.
- 24 A. Dabirian and R. Van de Krol, *Chem. Mater.*, 2015, **27**, 708.
- 25 P. W. Atkins, *The Elements of Physical Chemistry*, Oxford University Press, Oxford, U.K., 1996.
- 26 (a) F. Di Franco, M. Santamaria, F. Di Quarto, F. La Mantia, C. M. Rangel and A. I. De Sá, *ECS J. Solid State Sci. Technol.*, 2013, **11**, N205; (b) F. Di Franco, G. Zampardi, M. Santamaria, F. Di Quarto and H. Habazaki, *J. Electrochem. Soc.*, 2012, **159**, C33; (c) F. La Mantia, H. Habazaki, M. Santamaria and F. Di Quarto, *Russ. J. Electrochem.*, 2010, **46**, 1306.
- 27 A. Zaffora, F. Di Franco, M. Santamaria, H. Habazaki and F. Di Quarto, *Electrochim. Acta*, 2015, **180**, 666.
- 28 M. Santamaria, F. Di Quarto and H. Habazaki, *Electrochim. Acta*, 2008, **53**, 2272.
- 29 F. Di Quarto, M. Santamaria, P. Skeldon and G. E. Thompson, *Electrochim. Acta*, 2003, **48**, 1143.
- 30 M. Santamaria, F. Di Quarto, P. Skeldon and G. E. Thompson, *J. Electrochem. Soc.*, 2006, **153**, B518.
- 31 M. Santamaria, F. Di Quarto, S. Zanna and P. Marcus, *Electrochim. Acta*, 2011, **56**, 10533.
- 32 M. Santamaria, F. Di Quarto, S. Zanna and P. Marcus, *Electrochim. Acta*, 2007, **53**, 1315.
- 33 M. Santamaria, F. Di Franco, F. Di Quarto, P. Skeldon and G. E. Thompson, *J. Phys. Chem. C*, 2013, **117**, 4201.
- 34 F. Di Quarto, F. Di Franco, C. Monarca, M. Santamaria and H. Habazaki, *Electrochim. Acta*, 2013, **110**, 517.
- 35 N. F. Mott and E. A. Davis, *Electronic Processes in Non-crystalline Materials, 2nd Edition*, Clarendon Press, Oxford, U.K., 1979.
- 36 M. Santamaria, F. Di Quarto and H. Habazaki, *Corros. Sci.*, 2008, **50**, 2012.
- 37 F. Di Quarto, S. Piazza, M. Santamaria and C. Sunseri, in *Handbook of Thin Film Materials*, ed. H. S. Nalwa, Academic Press, New York, 2002, Vol. 2, Chapter 8, pp. 373–414.
- 38 (a) L. Onsager, *J. Chem. Phys.*, 1934, **2**, 599; (b) L. Onsager, *Phys. Rev.*, 1938, **54**, 554.
- 39 D. M. Pai and R. C. Enck, *Phys. Rev. B*, 1975, **11**, 5163.
- 40 O. S. Heavens, *Optical Properties of Thin Solid Films*, Dover Publications, New York, 1965.
- 41 D. R. Lide (ed.), *CRC Handbook of Chemistry and Physics, 90th Edition*, CRC Press/Taylor and Francis, Boca Raton, 2010.
- 42 S. Adachi, *The Handbook on Optical Constants of Metals*, World Scientific, 2012.